Numerical study of the impact of vaporisation on melt pool dynamics in Laser Powder Bed Fusion - Application to IN718 and Ti–6Al–4V

Alexis Queva, Gildas Guillemot, Clara Moriconi, Charlotte Metton, Michel Bellet

Additive Manufacturing 35 (2020) 101249

Contents lists available at ScienceDirect

Additive Manufacturing

journal homepage: www.elsevier.com/locate/addma

Numerical study of the impact of vaporisation on melt pool dynamics in Laser Powder Bed Fusion - Application to IN718 and Ti–6Al–4V

Alexis Queva[a,b,*], Gildas Guillemot[a], Clara Moriconi[b], Charlotte Metton[b], Michel Bellet[a]

[a] MINES ParisTech, PSL Research University, CEMEF - Centre de mise en forme des matériaux, CNRS UMR 7635, CS 10207 rue Claude Daunesse, 06904 Sophia Antipolis Cedex, France

[b] Safran Additive Manufacturing, a technology platform of Safran Tech, Rue des Jeunes Bois, Châteaufort, 78114 Magny-Les-Hameaux, France

ARTICLE INFO

Keywords:
Laser powder bed fusion
Metallic alloys
Numerical simulation
Vaporisation
Finite elements

ABSTRACT

A finite element model of Laser Powder Bed Fusion (LPBF) process applied to metallic alloys at a mesoscopic scale is presented. This Level-Set model allows to follow melt pool evolution and track development during building. A volume heat source model is used for laser/powder interaction considering the material absorption coefficients, while a surface heat source is used to consider the high laser energy absorption by dense metal alloys. An energy solver is applied considering convection and conductivity evolution in the system. Shrinkage during consolidation from powder to dense material is modelled by a compressible Newtonian constitutive law. An automatic remeshing strategy is also used to provide a good compromise between accuracy and computing time. Different cases are investigated to demonstrate the influence of the vaporisation phenomena, of material properties and of laser scan strategy on bead morphology.

1. Introduction

Interest is constantly growing for the manufacturing of aeronautical parts made by additive manufacturing (AM) processes [1]. These new processes bring a revolution in the design of parts. One of the most used AM technology is Laser Powder Bed Fusion (LPBF) whose principle is depicted in Fig. 1. Typically, the desired part is designed and prepared for build with a 3D CAD software. Thereafter, the geometry is sliced horizontally in layers with a thickness generally between 20 and 100 μm. Sprayed atomised powder is deposited with a roller or a recoater on the substrate or on the predeposited material.

Then, a high-power laser beam melts selectively the powder along the trajectories generated by the 3D model. A liquid domain is developed leading to a partial melting of the previous layers. The upper layer is rapidly solidified and bonded to the previous ones. The plateau goes down to receive the next layer spread by the recoater. These two steps are repeated until the final part is formed. The process operates in a protective atmosphere (typically argon) to avoid oxidation of the liquid metal and ensure final quality of manufactured parts. The LBPF process has several advantages over conventional forming techniques such as machining or casting. (i) Complex parts like lattice [2,3], foam [4] or fractal [5,6] structures can be manufactured. An example is encountered in the context of heat exchangers: fractal structures can improve performance both by increasing the exchange surface between hot and cold fluids and by generating small turbulent vortices in the hot fluid [5]. Furthermore, the mass of built parts is reduced [2] when optimising final shape. (ii) The manufacturing time is reduced since multi-components parts can be redesigned as a single part with AM technologies. (iii) The manufacturing cost with AM is lower compared to conventional techniques for small production volume. As an example, substantial investments have been made in aeronautical industries in order to develop LPBF processes and other related AM technologies [7]. Such investments come from other high-tech industries as encountered in medical, energy or spatial sectors [8,9].

Numerical simulation is an essential tool to achieve a better understanding of the various physical phenomena involved during PBF processes and their influences. For instance, as shown in Fig. 1, denudation [10,11] or vaporisation phenomena are observed during the process and strongly influence the final state of the built part [12,13]. In addition, LPBF process modelling provides assistance to investigate process parameter effects on part evolution during manufacturing in order to propose optimised solutions. Models have been developed in recent years mainly at macroscale (part-scale) and mesoscale (track/bead-scale). At the macroscale, Li and Gu [14] apply their model to a Ti–6Al–4V alloy and predict the temperature field by using a Gaussian heat source with temperature dependent material properties. They demonstrate that the heat is mainly extracted by conduction through the cold substrate. Hodge et al. [15] use a more complex heat source model

* Corresponding author.
E-mail address: alexis.queva@mines-paristech.fr (A. Queva).

https://doi.org/10.1016/j.addma.2020.101249
Received 15 November 2019; Received in revised form 11 February 2020; Accepted 26 March 2020
Available online 19 May 2020

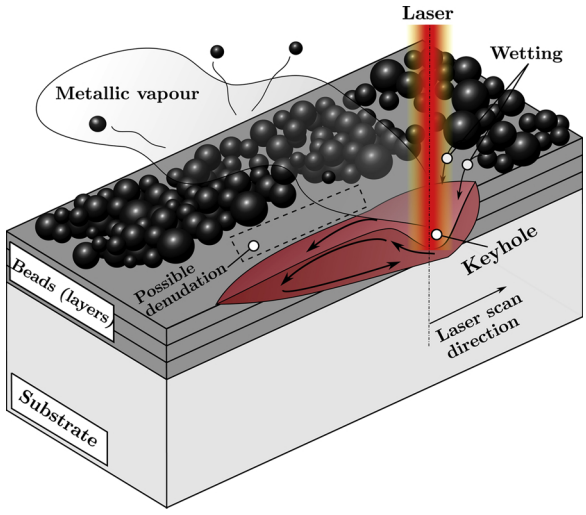

Fig. 1. Laser powder bed fusion – schematic of the multiple phenomena involved.

based on Gusarov's approach [16]. The thermal history and the cumulative plastic strain are obtained during the multilayer building. Van Belle et al. [17], Roberts et al. [18] and Marion et al. [19] have developed FEM based on birth and death technique for Direct Metal Deposition (DMD) modelling. Van Belle [17] shows the influence of the annealing temperature on the cumulative plastic strain and the resulting residual stresses in nickel-based alloys. Roberts et al. [18] and Marion et al. [19] use a heat source model considering the local absorption of laser energy in Ti–6Al–4V alloy. Finally, Zhang et al. [20] present an original and complex finite element model (FEM) applied to IN718 alloy. Both unmelted powder and surrounding gas domains are meshed. In addition, a dynamic mesh adaptation strategy is developed. The freshly sprayed layer to be melted is decomposed into several fractions that are heated consecutively. This original approach has been applied to simulate the building of a complex geometry. Interestingly, larger thermal gradients are encountered in the powder bed compared to the substrate due to the low thermal conductivity of powder.

Nevertheless, these models do not predict the shape of the tracks since the melt pool behaviour is not considered in such approaches. In the same way, the convective transport inside the melt pool and the latent heat effect associated with melting and solidification are neglected despite these phenomena have a great influence on heat transfer in the LPBF process. For these reasons, many authors developed models at a smaller scale (mesoscopic) to provide better estimations of local thermal gradients and bead shape morphologies. Particle-mesoscale models have been developped, using the discrete element method (DEM), or the FEM, coupled with CFD methods [12,21–25]. Bidare et al. [12] use a multiphysics model including laser plume and finally conclude that the laser plume velocity in LPBF process goes from 300 to 600 $m.s^{-1}$ (depending on the laser input energy in the Knudsen layer and decreases exponentially with height to a value close to 100 $m.s^{-1}$. Khairallah et al. [21] present a Lagrangian–Eulerian finite element approach applied to Ti–6Al–4V considering the powder bed as a set of compact random spheres. They demonstrate the importance and influence of the Marangoni effect. In addition, the recoil pressure associated to the keyhole development, due to the intense vaporisation, is taken into account. Its effect on the melt pool shape evolution is demonstrated. The model is able to compute the denudation phenomenon around the melt pool due to powder movement toward the melt pool. Martin et al. [22] use a similar approach and demonstrate the influence of laser turning points on the occurrence of porosities on the same alloy. Körner et al. [23] propose a numerical approach based on the lattice Boltzmann method. This latter approach allows them to simulate the manufacturing of single walls in 2D. The numerical results are compared with experimental measurements. They show that the surface forces and the density of packed powder bed are responsible for binding faults. Bayat et al. [24] show good experimental agreement on melt pool depth estimation when coupling resolution of heat conservation equations with the hydrodynamical solution. Aggarwal et al. [25] used a similar approach demonstrating the capability to get the transition from a conduction to a keyhole mode by reducing the laser spot radius with good agreement through experimental work. The main drawback of these particle-mesoscale models is that they are excessively time consuming since the computation of a surface representation including wetting effects is computer demanding [26]. For instance, Aggarwal et al. state that 120 hours are needed to compute a 0.75 mm track using 40 cores [25]. As a consequence, numerical simulations are generally limited to a single track or a single wall.

To avoid this numerical issue, an alternative approach consists in using continuous-mesoscale models, considering the powder as a continuous domain and not a discrete one [27,28]. This approach simplifies the computation of the moving interface in the material but requires the determination of homogenised material properties in the powder bed which have to be defined as functions of gas and bulk properties and considering its average porosity. Mukherjee et al. [27] have developed such a model. Their approach is suitable for modelling a multi-layer and multi-hatch building. In addition, applications are developed on different alloys to observe the influence of material properties on the bead shape. Nevertheless, this model does not consider the capillary effects such as surface tension and Marangoni forces. As a consequence, the exact morphology of the bead cannot be obtained.

In the present work, a continuous-mesoscale Level-Set model of the LPBF process is presented to follow melt pool evolution and track development during building. This FEM approach is based on previous developments by Chen et al. [28] to model ceramic materials evolution during LPBF process. The present paper provides an extension of this model to metallic materials, through several developments. Indeed, for ceramic materials with the laser wavelength generally used in AM by LBM, a single volume heat source is relevant to consider the low absorption of laser energy. However, the laser energy absorption is much more significant for metallic melt pool. Consequently, a modeling change for laser-metal interaction is required. Furthermore, some phenomena induced by vaporisation: release of latent heat in the thermal resolution and application of the recoil pressure in the mechanical resolution [12,13], which were not considered in Chen's approach, have to be considered. The heat source is modelled considering separately laser/melt pool and laser/powder interactions. A surface heat source is used to take into account the high laser energy absorption by dense metal alloys. In addition, a volume heat-source model is applied on the powder bed considering the material absorption coefficient. Like in Chen's approach [28], shrinkage during consolidation from powder to liquid is modelled by a compressible Newtonian constitutive law. The automatic remeshing strategy is used to provide a suitable compromise between accuracy and computational cost. Applications are developed both for IN718 and Ti–6Al–4V alloys since these materials are particularly suitable for aeronautics for their ability to provide good performance at high temperatures. Numerical cases of increasing complexity are investigated corresponding to i) a static laser shot, ii) a single track and iii) multiple-tracks to highlight the influence of hydrodynamic forces or material properties on the bead shape in a context of building lattice structures corresponding to very small-size beads. These results are not compared with experimental observations but illustrate how surface morphologies may vary, depending on material data and scanning strategy.

2. Numerical model

Material and gas domains are both included in a single system of interest. The powder bed is considered as continuous with a given porosity. The densification of the powder bed is a one-way

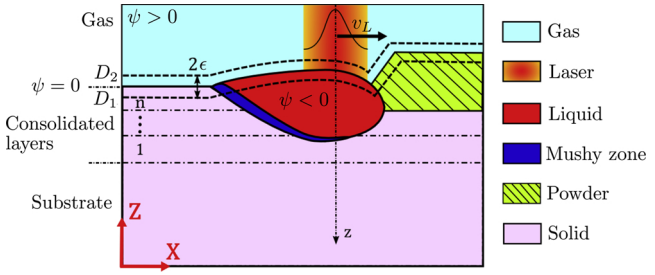

Fig. 2. Schematic of the LPBF process with the Level-Set (LS) method to track the interface associated to the isovalue $\psi = 0$ of the signed distance function.

transformation. No residual porosity is considered when powder is fully melted. In addition, both powder loss and projection are neglected. During the heating stage, the powder bed melts continuously to form a compact deposition on the substrate. This progressive transformation is modelled by a temperature-dependent powder fraction expression, also including a transition domain.

2.1. Level-set method

The material domain, D_1, and gas domain, D_2, are shown in Fig. 2. The Level-Set method is used to track the evolution of the gas/material interface [29]. A signed distance function ψ is used respecting the eikonal condition $||\nabla\psi|| = 1$.

This function is arbitrarily chosen positive in a domain and consequently negative in the other. For instance, this function is considered positive in the gas domain in the present approach as shown in Fig. 2. A transition zone with half thickness ε is used to compute the Heaviside function $\mathscr{H}$ defined as:

$$\mathscr{H}(\psi) = \begin{cases} 0 & \psi < -\varepsilon \\ \frac{1}{2}\left[1 + \frac{\psi}{\varepsilon} + \frac{1}{\pi}\sin\left(\frac{\pi\psi}{\varepsilon}\right)\right] & |\psi| \le \varepsilon \\ 1 & \psi > \varepsilon \end{cases} \tag{1}$$

A continuous evolution of physical properties at the material/gas interface is made possible considering this Heaviside function. For any given property χ, the property is firstly averaged between phases by their volume fractions in each domain D_i, according to the concept of Representative Elementary Volume [30]:

$$\langle\chi\rangle^{D_i} = \sum_{\phi} g_{D_i}^{\phi}\chi^{\phi} \quad \forall\, i \in \{1, 2\} \tag{2}$$

where $g_{D_i}^{\phi}$ is the volume fraction of phase ϕ in the domain D_i and χ^{ϕ} is the intrinsic value associated to property χ in the phase ϕ. Then, the global property $\{\chi\}$ is averaged between the two domains by the Heaviside function, in particular in the transition zone around the D_1/D_2 interface [31,32]:

$$\{\chi\} = \mathscr{H}\langle\chi\rangle^{D_2} + (1 - \mathscr{H})\langle\chi\rangle^{D_1} \tag{3}$$

The Dirac function, δ, can be derived from the Heaviside function as:

$$\delta(\psi) = \frac{\partial\mathscr{H}(\psi)}{\partial\psi} = \begin{cases} \frac{1}{2\varepsilon}\left[1 + \cos\left(\frac{\pi\psi}{\varepsilon}\right)\right] & |\psi| \le \varepsilon \\ 0 & |\psi| > \varepsilon \end{cases} \tag{4}$$

This function will be used to convert surface mechanical loads along the gas/metal interface into volume loads applied within the 2ε-thick neighbourhood of the interface. Finally, the evolution of the interface position is tracked by a two-step procedure. First, the resolution of the transport equation of this distance function is developed as (5) :

$$\frac{\partial\psi}{\partial t} + \mathbf{u}\cdot\nabla\psi = 0 \tag{5}$$

where $\mathbf{u}$ is the velocity field induced by the powder shrinkage and the melt pool evolution. Then, a geometric reinitialisation method is used in order to compute the distance function with respect to the eikonal condition after transport [33]. Finally, considering that the Level-Set method involves mass conservation issues, a method developed by Zhang et al. [34] has been used to overcome this drawback.

2.2. Governing equations

2.2.1. Energy conservation and heat source modelling

The modelling of heat transfer in LPBF is obtained as the solution of the non-steady equation for energy conservation [24,28]:

$$\frac{\partial\{\rho h\}}{\partial t} + \nabla\cdot(\{\rho h\}\mathbf{u}) - \nabla\cdot(\{\lambda\}\nabla T) = \dot{q}_L - \dot{q}_v \tag{6}$$

where ρ is the density, h the specific enthalpy, λ the thermal conductivity and T the temperature. $\dot{q}_L$ represents the heat source associated with the laser, while $\dot{q}_v$ denotes the heat loss associated to vaporisation (detailed further).

Heat source modelling. The laser follows a radial Gaussian distribution considering a reflection coefficient R (or an absorptivity coefficient $(1 - R)$). Consequently the heat flux at the upper surface, $\phi_0(r, r_0)$, is given by the following expression:

$$\phi_0(r, r_0) = (1 - R)\,\frac{2P_L}{\pi r_0^2}\,\exp\left(-\frac{2r^2}{r_0^2}\right) \tag{7}$$

where P_L is the laser power and r_0 is a specific radius depending on the state of the material where laser radiations interact. Two cases should be considered depending on the state of the surface, as depicted in Fig. 3.

The first case corresponds to the interaction between the laser and the powder bed (i.e. laser/powder interaction). Multiple reflections occur due to the interactions between powder particles and radiations when the laser progressively penetrates the powder bed. Considering these reflections, the heat source associated to powder $\dot{q}_L^p$ can be expressed with a volume formulation. Complex expressions are used in the literature, which take into account the number of particles or the albedo [35,36]. In the present work, a Beer–Lambert law is considered where the heat source is equal to the flux variation in the propagation direction z [28,37]:

$$\dot{q}_L^p(r, z) = \phi_0(r, r_{\text{int}})\ \alpha\ \exp\left(-\int_0^z \alpha\,\mathrm{d}l\right) \tag{8}$$

where r_{int} is the interaction radius and α is the local value of the

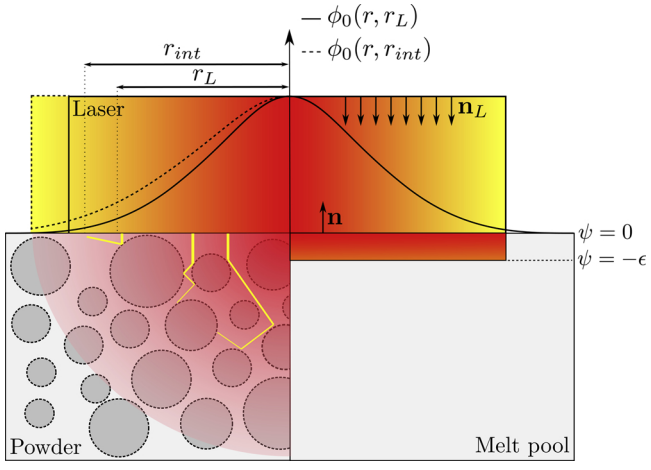

Fig. 3. The laser/powder interaction model is represented on the left, considering multiple reflections between particles. The laser/dense matter interaction occurring at the melt pool surface is represented on the right side with a surface term due to high absorption of laser energy.

absorption coefficient. It should be emphasised that the multiple reflections phenomenon leads to an enlargement of the interaction radius ($r_{\text{int}} > r_L$).

The second case corresponds to the interaction between the laser and the dense matter (in practice, the melt pool). As a result of the high absorption of dense metals, the heat source is expressed with a surface formulation. However, in the Level-Set context, the surface heat source is converted into a volume heat source by use of the Dirac function [38]:

$$\dot{q}_L^d(r, z) = \phi_0(r, r_L)\ \cos(\theta)\ \delta_2(\psi) \tag{9}$$

where r_L is the nominal laser radius and θ is the angle between $\mathbf{n}$, the normal of the gas/melt pool interface and $\mathbf{n}_L$, the fixed laser direction. The direct use of the Dirac function δ (Eq. (4)) would introduce undesirable heat into the gas when it should essentially be restricted to the dense material. Alternative expressions can be considered. In this work, the following δ_2 function will be used (Eq. (10)).

$$\delta_2(\psi) = \begin{cases} 0 & \text{if } \psi > 0 \\ 2\delta(\psi) & \text{if } \psi \leq 0 \end{cases} \tag{10}$$

If the laser power irradiates concurrently the melt pool and the powder bed, the heat source applied is deduced from the liquid fraction value to ensure that the laser energy is provided correctly:

$$\dot{q}_L = (1 - g_l)\ \dot{q}_L^p + g_l\ \dot{q}_L^d \tag{11}$$

where g_l is the volume liquid fraction. Since solidification occurs under high temperature gradient, the evolution of the volume liquid fraction is oversimplified by evolving linearly with temperature during the melting/solidification path:

$$g_l = \begin{cases} 0 & T < T_s \\ \dfrac{T - T_s}{T_l - T_s} & T_s \leq T \leq T_l \\ 1 & T_l < T \end{cases} \tag{12}$$

where T_s and T_l correspond respectively to the solidus and liquidus temperature.

Vaporisation heat loss modelling. The plume of metal vapour is not taken into account in the model since this would require a considerable modelling effort and would result in significant undesired numerical constraints [12,13]. In the present paper, only consequences of vaporisation are considered and modelled in terms of heat transfer (hereunder) and momentum conservation (next section).

When the temperature exceeds the boiling temperature T_v, the energy loss due to the ejection of metallic vapours is modelled by a volume heat sink $\dot{q}_v$ [21,39,40]:

$$\dot{q}_v = (1 - \beta_r)\sqrt{\frac{M}{2\pi RT}}\ p_0\ exp\left(\frac{L_v M}{RT_v}\left(\frac{T - T_v}{T}\right)\right) L_v\ \delta_2(\psi) \tag{14}$$

where represents the vaporisation rate in mass per unit surface and unit time. β_r is the retrodiffusion coefficient assumed equal to 0.17 [21,24], M is the molar mass of the alloy, R the universal gas constant, p_0 is the atmospheric pressure and L_v is the latent heat of vaporisation per unit mass. The retrodiffusion coefficient β_r represents the percentage of metallic vapour surrounding the liquid/vapour interface, more precisely in the Knudsen layer [41], which returns to the melt pool. Thus, a low value of this coefficient means that metallic vapour tends to leave the melt pool (high vaporisation state). On the contrary, a high value of the retrodiffusion coefficient signifies that particles have a strong tendency to return by recondensation to the melt pool. Klassen et al. [41] determine that this coefficient is defined as a function of the Mach number at the Knudsen layer and vary between 1 down to 0.17. Furthermore, Bidare et al. [12] and Khairallah et al. [21] outline that the Mach number around the Knudsen layer is at least close to the sonic state and explained consequently the choice of this value (0.17) for the retrodiffusion coefficient in the present approach.

2.2.2. Momentum conservation

The convective flow has a major influence on the temperature field and the melt pool shape. Fluid dynamics equations are established by the mass and momentum conservation equations. A compressible Newtonian flow behaviour has to be considered in order to assume the change of apparent density in the powder bed during the melting stage [28]:

$$\nabla\cdot\mathbf{u} = \dot{\theta} = -\frac{1}{\{\rho\}}\frac{d\{\rho\}}{\mathrm{d}\,t} \tag{15}$$

$$\{\rho\}\left(\frac{\partial \mathbf{u}}{\partial t} + (\mathbf{u}\cdot\nabla)\mathbf{u}\right) - \nabla\cdot\left(2\{\mu\}\left(\bar{\bar{\varepsilon}} - \frac{1}{3}\mathrm{tr}(\bar{\bar{\varepsilon}})\bar{\bar{\mathbf{I}}}\right) - p\bar{\bar{\mathbf{I}}}\right) = \mathbf{f}_V \tag{16}$$

where $\dot{\theta}$ is the negative volume expansion rate associated with the transition from powder to dense material, μ is the dynamic viscosity, $\bar{\bar{\varepsilon}}$ is the strain rate tensor, $\bar{\bar{\mathbf{I}}}$ is the identity tensor and $\mathbf{f}_V$ are the volumetric forces. The dynamics of the melt pool have several origins: i) the capillary effects driven by surface tension $\mathbf{f}_V^{\text{STn}}$ and Marangoni forces $\mathbf{f}_V^{\text{STt}}$; ii) the recoil pressure $\mathbf{f}_V^{\text{RPn}}$ during the vaporisation phase which induces the deflection of the interface by the high velocity of ejected metal vapour; iii) the buoyancy forces $\mathbf{f}_V^g$ due to the local variation of density with temperature. This set of forces are all considered in the present modelling. Consequently, the volumetric force is written as the sum of these forces respectively as:

$$\mathbf{f}_V = \mathbf{f}_V^{\text{STn}} + \mathbf{f}_V^{\text{STt}} + \mathbf{f}_V^{\text{RPn}} + \mathbf{f}_V^g \tag{17}$$

Capillary forces. The main driving forces for the convection of the melt pool are capillary forces. Chen shows that these forces have a major influence on the evolution of the capillary front and on the melt pool shape [42]. The surface tension force represents the action of gas molecules on the liquid to minimise the interface energy. This force is directed toward the liquid at the liquid/gas interface for negative curvature and tends to bend the liquid consequently:

$$\mathbf{f}_V^{\text{STn}} = \gamma(T)\ \kappa\ \delta^{\text{ST}}\ \mathbf{n} \tag{18}$$

The surface tension coefficient, γ, is considered highly dependent on temperature with the following linear relation:

$$\gamma(T) = \gamma_l + \frac{\partial\gamma}{\partial T}(T - T_l) \tag{19}$$

where γ_l is the value of the surface tension coefficient at the liquidus temperature T_l, $\kappa = -\nabla\cdot\mathbf{n}$ represents the curvature of the interface with $\mathbf{n} = \frac{\nabla\psi}{\|\nabla\psi\|}$ the unit normal vector, and δ^{ST} is a Dirac function defined similarly as Eq. (4). However, this function is computed with a separate Level-Set function associated to the liquid/gas and liquid/powder interface as shown in Fig. 4(a). Chen et al. [28] detail the numerical method used to compute surface tension forces on these interfaces.

Due to the high temperature gradient in the melt pool, shear stress at the liquid/gas interface occurs and modifies drastically the convection. This phenomena is due to the Marangoni effect corresponding to change in the magnitude of the surface tension coefficient. These

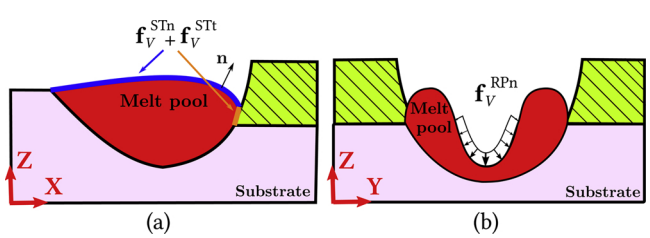

Fig. 4. (a) Surface tension and Marangoni forces are applied on the liquid/gas interface (blue) and at the liquid/powder interface (yellow). (b) Spatial distribution of the recoil pressure force.

Table 1
Material properties for IN718 and Ti–6Al–4V alloys.

Property	Symbol	Value		Units	Ref
		IN718	Ti–6Al–4V		
Reflection coefficient	R	0.7	0.7		[56]
Solidus temperature	T_s	1170	1536	°C	[57]
Liquidus temperature	T_l	1336	1636	°C	[57]
Boiling temperature	T_v	2913	3336	°C	[57]
Density of solid phase	ρ_s	8190	4200	kg . m^{-3}	[57]
Density of solid phase	ρ_l	7300	3900	kg . m^{-3}	[57]
Heat capacity of solid phase	$C_{p,s}$	512	550	J . kg^{-1}. K^{-1}	[57]
Heat capacity of liquid phase	$C_{p,l}$	720	895	J . kg^{-1}. K^{-1}	[57]
Latent heat of fusion	L_f	270	286	kJ . kg^{-1}	[57]
Latent heat of vaporisation	L_v	6300	8890	kJ . kg^{-1}	[24,58]
Thermal conductivity of dense material	λ_d	Fig. 5(a)	Fig. 5(a)	W . m^{-1}. K^{-1}	[57]
Thermal conductivity of powder bed	λ_p	Fig. 5(a)	Fig. 5(a)	W . m^{-1}. K^{-1}	[59]
Absorption coefficient of powder bed	$\langle\alpha_p\rangle$	25	25	m^{-1}	
Surface tension coefficient	γ_l	1.89	1.42	N . m^{-1}	[57]
Marangoni coefficient	$\partial\gamma$ / ∂T	$-1.1\cdot10^{-4}$	$-2.48\cdot10^{-4}$	N . m^{-1}. K^{-1}	[57]
Dynamic viscosity (powder/dense material)	μ (μ_p/μ_d)	Fig. 5(b)	Fig. 5(b)	Pa.s	

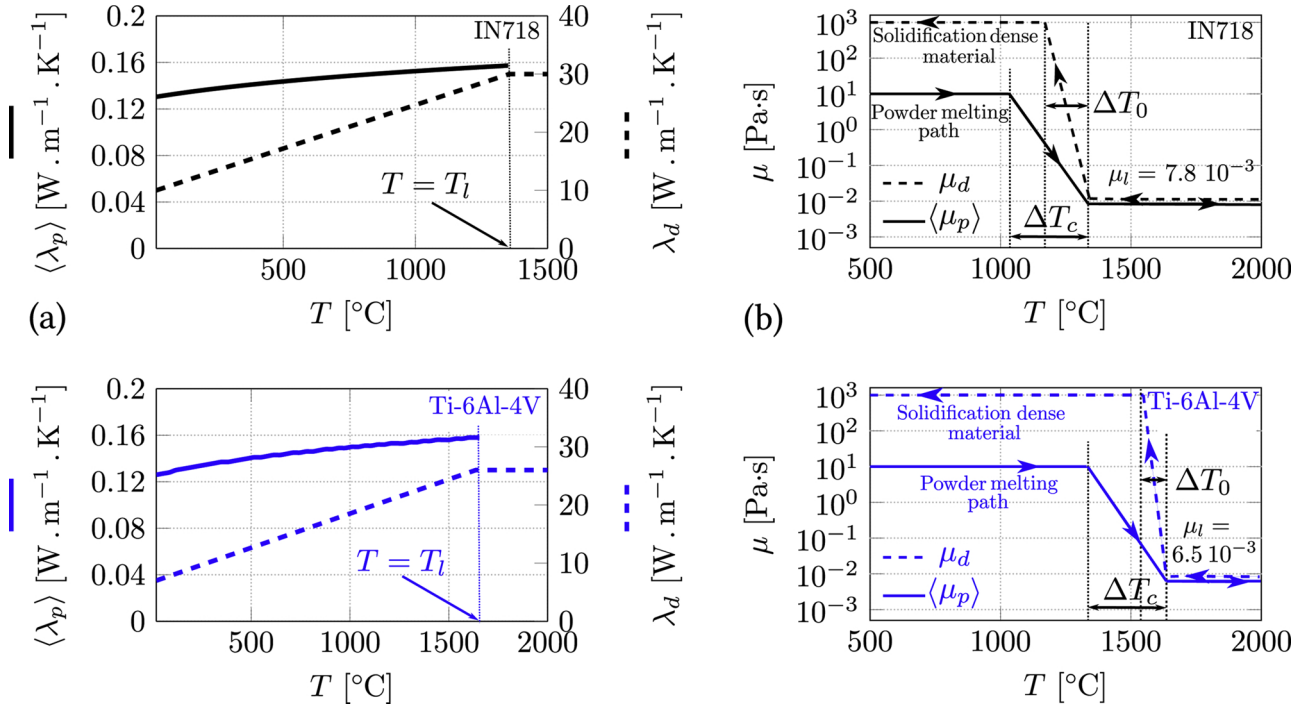

Fig. 5. (a) Thermal conductivity evolution of the bulk and the powder bed with temperature. (b) Dynamic viscosity as a function of temperature for the two alloys investigated (IN718 and Ti–6Al–4V).

evolutions are induced by temperature evolution at the liquid/gas interface. The associated volume force is expressed by:

$$\mathbf{f}_V^{\mathrm{STt}} = \frac{\partial\gamma}{\partial T}\,\nabla_S T\;\delta^{\mathrm{ST}} \tag{20}$$

where $\nabla_S T$ represents the thermal surface gradient (i.e. the tangential component of the temperature gradient at the interface) defined as $\nabla_S T = \nabla T - (\nabla T\cdot\mathbf{n})\mathbf{n}$.

Recoil pressure force due to vaporisation. During vaporisation, an intense ejection of metallic vapours is generated. This ejection implies an action/reaction mechanism inducing a force towards the liquid that deforms the melt pool surface inwards and allows the laser energy to penetrate deeper into the material. In the literature [21,24], this force is expressed proportionally to the saturated vapour pressure at the liquid/gas interface as shown in Fig. 4(b):

$$\mathbf{f}_V^{\mathrm{RPn}} = -\left(\frac{1+\beta_r}{2}\right) p_0\,\exp\left(\frac{L_v M}{\mathrm{RT}_v}\left(\frac{T-T_v}{T}\right)\right)\delta\;\mathbf{n} \tag{21}$$

This force is responsible for keyhole at high input linear laser energy [43,44].

Buoyancy force. Finally, the dependency of the density with temperature generates buoyancy forces expressed as:

$$\mathbf{f}_V^{g} = \{\rho\}\mathbf{g} \tag{22}$$

where $\mathbf{g}$ is the acceleration due to gravity.

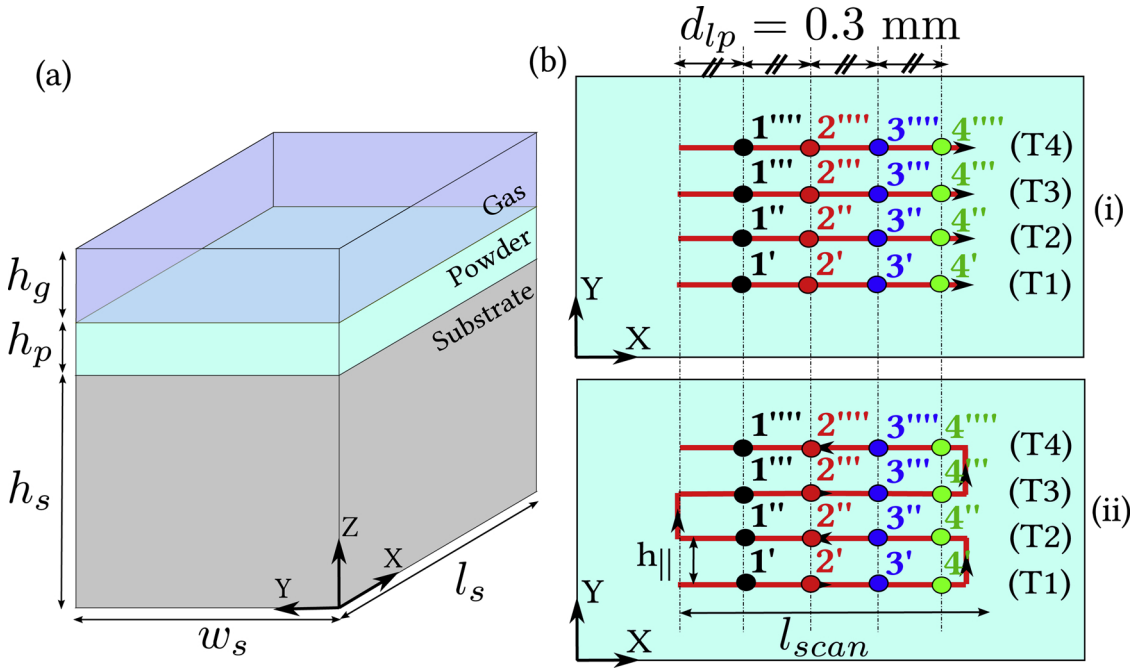

Fig. 6. (a) Simulation domain and associated dimensions in Table 2. (b) Configurations in multiple single tracks with an (i) unidirectional and (ii) alternate scanning with the sixteen local points where the temperature field is retrieved (20 μm deep in the substrate, $Z = 0.94$ mm).

Table 2
Domain sizes and machine settings for all configurations investigated.

Parameters		Units	SLS	ST − MT
Domain size	w_s	[mm]	1.00	2.00
	l_s	[mm]	1.00	2.50
	h_s	[mm]	0.95	0.96
	h_g	[mm]	0.10	0.10
Machine settings	P_L	[W]	250	285
	r_{int}	[μm]	50	50
	r_L	[μm]	50	42
	v_L	[m . s^{-1}]	/	1.0
	h_p	[μm]	50	40
	$h_{\|\|}$	[μm]	/	110
	l_{scan}	[mm]	/	1.25

Table 3
Boundary conditions for thermal and mechanical resolutions

Zones	Thermal	Fluid
Lateral faces	Adiabatic	$\mathbf{u}\cdot\mathbf{n} = 0$
Bottom	Adiabatic	$\mathbf{u}\cdot\mathbf{n} = 0$
Top	Free	Free

Table 4
Argon gas properties.

Property	Symbol	Value	Units	Ref
Density	ρ_g	1.3	kg . m^{-3}	[60]
Heat capacity	$C_{p,g}$	520	J . kg^{-1}. K^{-1}	
Thermal conductivity	λ_g	0.025	W . m^{-1}. K^{-1}	[60]
Viscosity	μ_g	10^{-4}	Pa. s	
Absorption coefficient	α_g	0	m^{-1}	

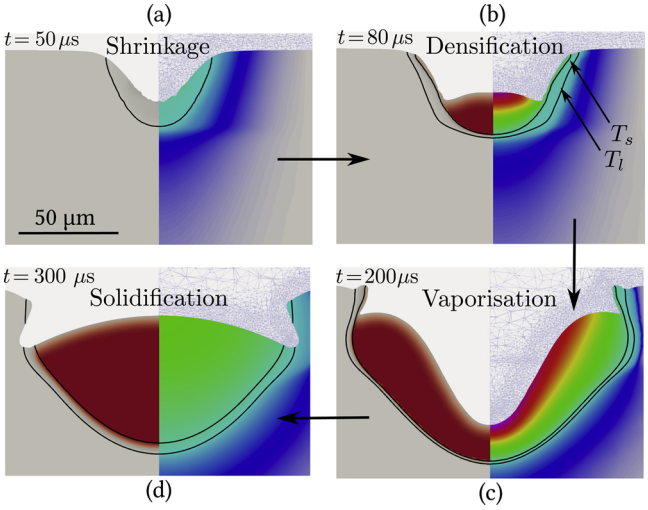

Fig. 7. Successive stages during laser-matter interaction: (a) shrinkage of the powder. (b) Densification of the powder into a melt pool. (c) Vaporisation stage with recoil pressure. (d) Interruption of the laser / Beginning of the solidification.

2.3. Numerical methods

As previously mentioned, the finite element method is used to solve the different equations which are loosely coupled.

2.3.1. Energy conservation

The energy conservation equation is solved in the whole system (matter and gas) using a preexisting FE solver [45]. This solver is based on a non-linear temperature resolution using a tabulated phase transformation and tabulated phase properties. Phase changes are consequently modelled both during heating and cooling stages considering this general description.

The volume heat source is computed as explained previously in Section 2.2.1. The spatial integration of the absorption (Eq. (8)) is computed on a regular grid with a trapezoidal rule. These values are then mapped onto the non-structured FE mesh.

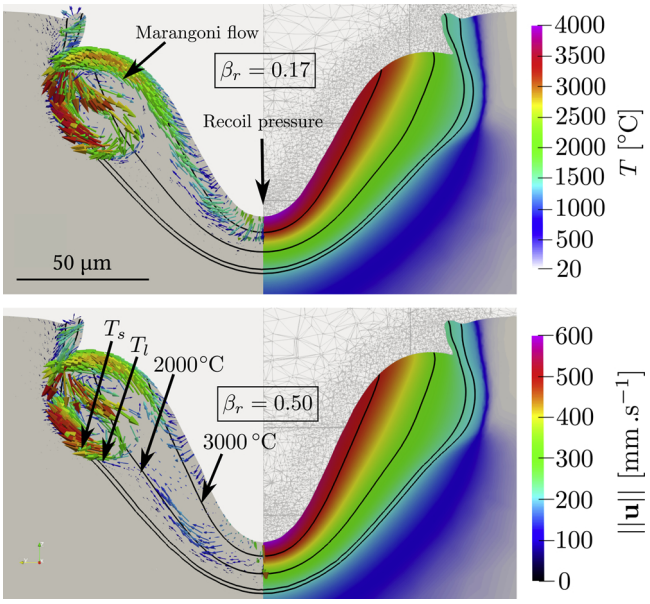

Fig. 8. Snapshot at t= 200 μs of the melt pool shape for two different values of β_r (0.17 and 0.50).

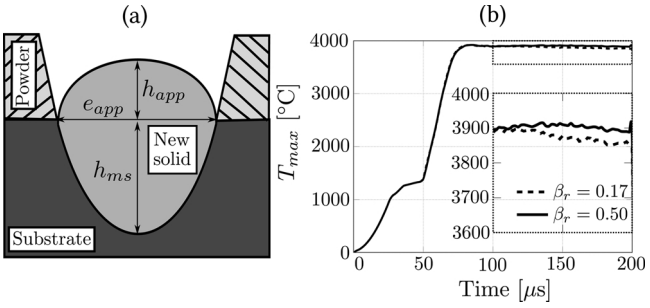

Fig. 9. (a) Dimensions of the solid shape investigated. (b) Temporal evolution of the maximum of temperature in the melt pool for two different values of β_r (0.17 and 0.50).

Table 5
Dimensions of the newly formed solid after laser shooting for two different values of β_r (0.17 and 0.50).

Dimensions	β_r = 0.17	β_r = 0.50	|Deviation| [%]
h_{app}	32	31.1	4.06
h_{ms}	43	50.2	16.74
e_{app}	140	141	0.71

2.3.2. Momentum conservation

For the computation of momentum conservation equation, a Variational MultiScale (VMS) method is chosen. This method was initially proposed by Tezduyar et al. [46,47]. The solver consists of a stabilised P1 formulation and results from developments conducted by Gouttebroze [48,49] and Hachem et al. [50,51]. A slight modification in the VMS formulation has been implemented to consider the shrinkage of the powder bead when transformed into a compact medium [28]. Concerning the capillary forces and more precisely the computing of the curvature, Brackbill et al. [38] demonstrated that prohibitive numerical limitations are encountered if these forces are fully explicitly treated. Consequently, the present model relies on former works by Hamide [52] and Khalloufi [53], who developed a semi-implicit treatment of the curvature computation to reduce this limitation.

2.3.3. Remeshing strategy

As the computational cost with FE methods is highly dependent on the number of degrees of freedom, an optimised and adapted mesh is required to get sustainable CPU times. Indeed, even if there are extra costs when using adaptative remeshing (such as metric calculation, remeshing and transport of fields from old to new mesh), the gains by coarsening and refining locally the mesh where it is useful remain predominant compared to the use of a static mesh. Consequently, a dynamic remeshing strategy is developed to follow the spatial evolution of the gas/material interface, the liquid fraction or the heat source term. In the present model, an anisotropic mesh controlled by a suitable multi-objective metric is used. Indeed, the metal/gas interface, the mushy zone or the laser heat source input have to be finely meshed for good accuracy. This method was initially developed by Coupez [54,55] and is based on an error estimation related to selected solution fields. Zones where the Hessian (second spatial derivative) of these fields is high are consequently finely remeshed.

3. Application to LPBF configurations

3.1. Configuration and material properties

Increasingly complex simulations are investigated in a building context with the LPBF process:

- A static laser shot (SLS) on a IN718 powder bed to identify the different stages during the process and to investigate the influence of the retrodiffusion coefficient β_r on the simulation process;
- A single track (ST) on a IN718 powder bed to investigate the influence of the vaporisation phenomena on the bead shape;
- Multiple tracks (MT) on IN718 and Ti–6Al–4V powder bed with different laser scan strategies (Fig. 6(b)) in a context of a lattice structure (very thin layer) building to understand their influences on the shape of the beads.

The whole system is described in Fig. 6. The substrate has overall dimensions $l_s \times w_s \times h_s$ evaluated in Table 2. The powder layer and gas thicknesses are denoted h_p and h_g. For the MT case, the laser trajectory follows a unidirectional or alternate scanning pattern with hatch distance $h_{||}$ equal to 110 µm.

The system dimensions are chosen so that the boundary conditions expressed in Table 3 are fulfilled. The physical properties of the different alloys investigated and the gas are described in Tables 1 and 4. The properties of the gas are those from argon [60]. The gas absorption coefficient is assumed equal to zero.

The laser considered in this study is a Yb: YAG with wavelength λ_L = 1070 nm. The reflection coefficient R used for the laser heat source model (7) is highly dependent on the laser wavelength [61]. According to the literature, a relevant value of the reflection coefficient in a laser-metal interaction context with this wavelength is 0.3 [56]. At the beginning of the building of each single track, the power of the heat source is progressively introduced from 0% to 100% of effective power with the following expression:

$$\dot{q}_L^{\text{simulation}} = \left(1 - \exp\left(-\frac{t}{\tau}\right)\right) \dot{q}_L \tag{23}$$

where $\tau = r_L/v_L$ and v_L is the laser scan velocity.

As the powder bed is considered as a continuous medium, equivalent material properties need to be provided to the powder. For example, the apparent density of the powder bed ρ_p is obviously expressed as a function of the apparent density of the bulk ρ_d and the average porosity of the powder bed ϕ_p:

$$\langle \rho_p \rangle = \langle \rho_d \rangle (1 - \phi_p) \tag{24}$$

The equivalent thermal conductivity of the powder is more complex to

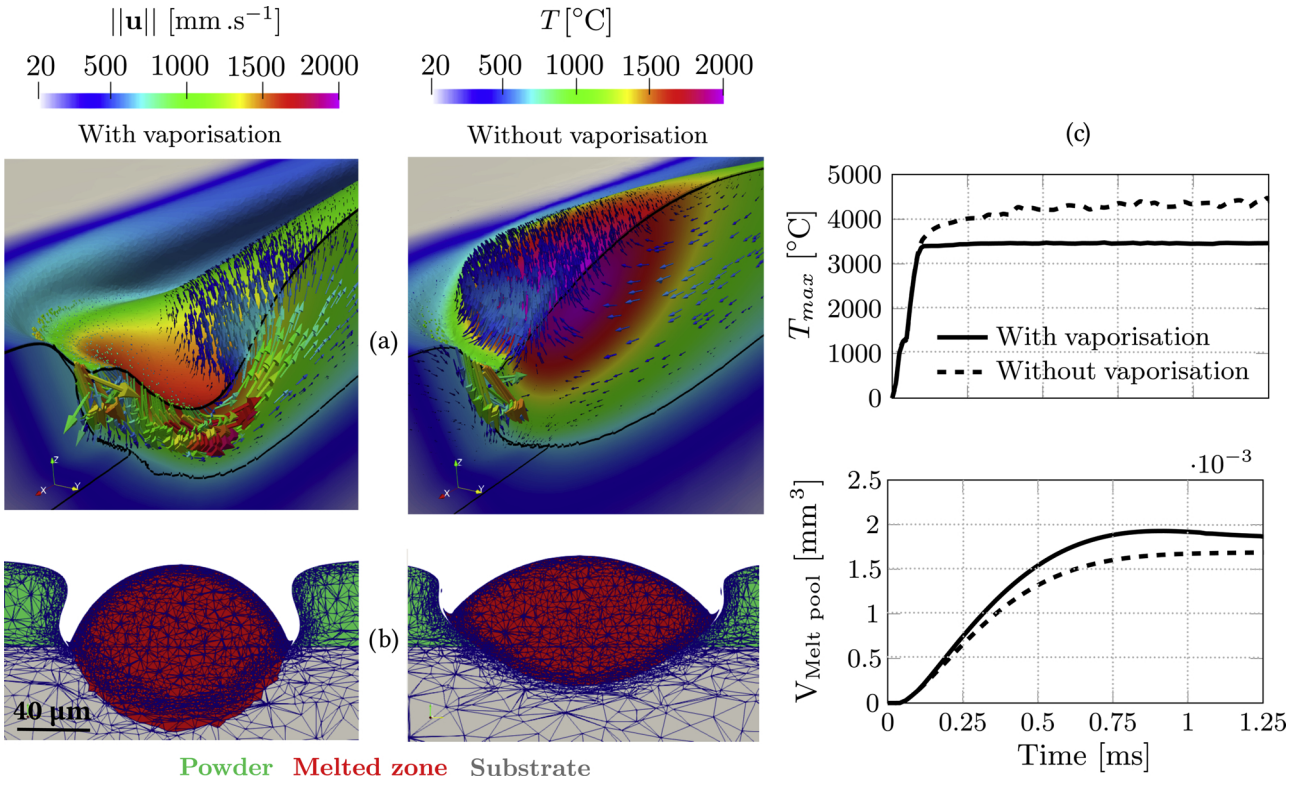

Fig. 10. (a) Zoom on the laser-matter interaction zone. (b) 2D transversal section at $Y = 0.8$ mm. (c) Temporal evolution of the maximum temperature in the dense matter and the volume of the melt pool.

Table 6
Dimensions of the solid bead after the laser shooting for the two different configurations investigated (case 1 and case 2).

Dimensions	Case 1	Case 2	|Deviation| [%]
h_{app}	38.1	39.4	3.4
h_{ms}	43	19	55.8
e_{app}	108	128	18.5

Table 7
Adimensional terms values for IN718 where L_c is the characteristic length chosen as 150 µm (melt pool width) and α_T is the thermal diffusivity coefficient.

Number	Notation	Definition	Value
Bond	Bo	$\frac{\Delta\rho\ g\ L_c^2}{\gamma_l}$	≈ 0.001
Prandtl	Pr	$\frac{\mu_l\ C_p}{\lambda_d}$	≈ 0.2
Reynolds	Re	$\frac{\rho_l\ \|\|\mathbf{u}\|\|\ L_c}{\mu_l}$	≈ 500
Marangoni	Ma	$\left(\frac{\partial\gamma}{\partial T}\right)\frac{L_c\ \Delta T}{\mu_l\ \alpha_T}$	≈ 800

determine. An analytical law proposed by Zehner and Schlünder [59] is used to have access to this estimation. This law takes into account the thermal conductivity of the bulk, λ_d, and of the gas, λ_g, the powder bed porosity, non-linear contacts and radiative effects between the powder particles:

$$\frac{\langle\lambda_p\rangle}{\lambda_g} = 1 - \sqrt{\bar{\phi}_p} + \frac{2\sqrt{\bar{\phi}_p}}{1-\beta B}\left[\frac{(1-\beta)B}{(1-\beta B)^2}\ln\left(\frac{1}{\beta B}\right) - \frac{B+1}{2} - \frac{B-1}{1-\beta B}\right] \tag{25}$$

where $\bar{\phi}_p = 1 - \phi_p$, $\beta = \lambda_g/\lambda_d$ and $B = 1.25\ (\bar{\phi}_p/\phi_p)^{10/9}$.

The absorption coefficient of the powder α_p is arbitrarily set to 25 mm^{-1} ($1/\alpha_p \approx h_p$). Consequently the laser input energy is mainly absorbed in the whole powder bed thickness due to multiple reflections. The thermal conductivity of the bulk and the powder bed are expressed in Fig. 5(a) depending on temperature.

The dynamic viscosity is assumed to have stable values at low temperature respectively equal to 10 Pa.s and 1000 Pa.s for both powder and dense matter. These values evolve later at higher temperature: the powder viscosity progressively decreases when attaining the solidus temperature with a densification domain $\Delta T_d = 300$°C (Fig. 5(b)). This domain is larger than the phase change domain associated to the alloy due to numerical issues [28]. A similar decrease is proposed for the dynamic viscosity evolution associated to the dense matter, however, restricted to the melting/solidification domain. Liquid viscosity is then reached when temperature exceeds the liquidus temperature (Fig. 5(b)). Moreover, the model considers powder densification as a one-way transformation.

4. Results and discussions

4.1. Static shot applied to IN718

The first case investigated is a static laser shot on a powder bed of IN718 with a porosity of 50 % (fixed for all cases). The laser power is equal to 250 W with a radius of 50 μm(Table 2). Different stages of the process are predicted by the model as shown in Fig. 7.

First, the powder shrinkage induced by the high laser input energy and temperature increase generates a decrease in thickness of the powder bed before getting a dense medium (Fig. 7(a)). A melt pool progressively develops at larger temperature in the bottom part (Fig. 7(b)). Then, the melt pool extends due to the progressive melting of powder. Once the melt is fully developed, the spheroidisation of the melt pool is achieved by surface tension effect. During the laser shot, the temperature and thermal gradient increase. Thus, the Marangoni forces intensify and enlarge the melt pool. When the temperature

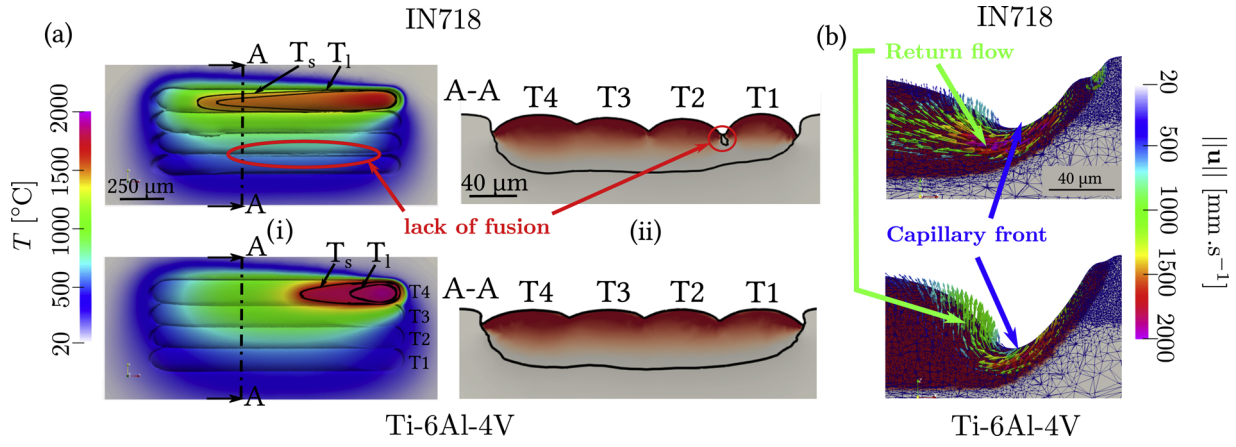

Fig. 11. (a) Snapshots after the almost solidification of a 4-track layer (unidirectional scan) with (1) top view and (2) transversal section. The black isocontour line represents the boundary of the melted zone. (b) Longitudinal section at t = 2.432 ms with the melted zone in red and the velocity field.

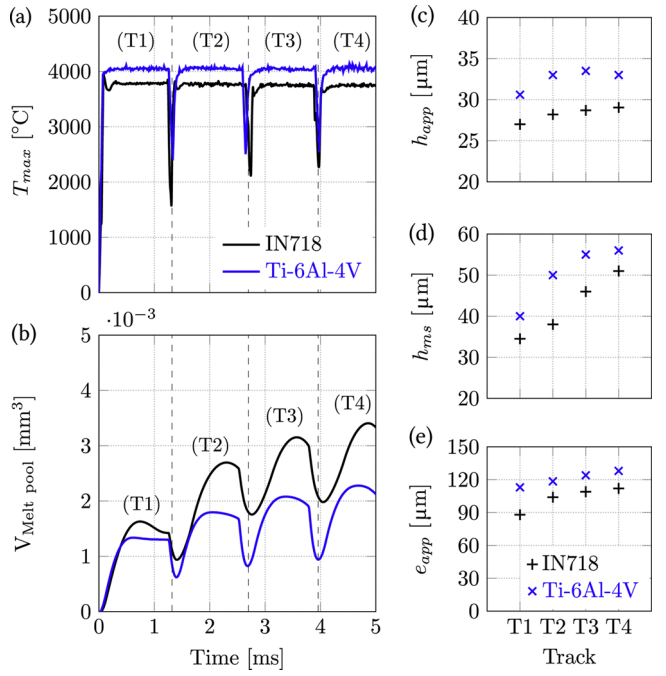

Fig. 12. (a-e) Temporal evolution of the maximum temperature in the dense matter, the volume of the melt pool and the dimensions of the melt pool (h_{app}, h_{ms} and e_{app}) at X = 1.25 mm.

exceeds the boiling temperature, the recoil pressure deflects the melt pool and consequently significantly modifies its shape (Fig. 7(c)). Finally, when the laser stops, the recoil pressure which was counterbalancing the surface tension force disappears implying a significant raise of the melt pool by surface tension effect (Fig. 7(d)). High temperature gradients around 5×10^7 °C·m^{-1} are observed in Fig. 8, which lead to significant Marangoni forces. In addition, two different values of β_r are used in the present simulations in order to investigate the retrodiffusion coefficient effect on melt pool evolution. Indeed, a coefficient equal to 0.17 is firstly used as proposed in the present model. Secondly, a value of 0.50 provided in the literature [62] is chosen to compare maximum temperature evolution and saturation pressure obtained in the melt pool.

As shown in Fig. 9(b), The maximum temperature observed is largely greater than the boiling temperature of the IN718 alloy in both cases. When the value of the retrodiffusion coefficient is higher, the vaporisation of the metal is lower. Slightly higher temperatures are consequently observed in the melt pool as the heat sink source term decreases with β_r as shown in Fig. 9(b). The maximum temperature as shown in Fig. 9(b) is approximately 50 °C higher when the retrodiffusion coefficient is higher than the one typically chosen in litterature [21,24]. Even if the difference of maximum temperature are not significant, it induces a non-negligible difference value of recoil pressure, due to the Clapeyron expression (Eq. (21)), and consequently changes the dimensions of the melt pool as shown in Fig. 8.

As shown in Table 5, the melt pool depth h_{ms} increases when β_r increases due to stronger recoil pressure forces (approximately 28% stronger for β_r = 0.5 than for β_r = 0.17). This gap between the two cases can increase if a higher laser power is used. Therefore, the dimensions of the melt pool are highly dependent on the vaporisation phenomena. The maximum in velocity magnitude observed in this simulation is close to 0.75 m . s^{-1}. The non turbulence hypothesis is consequently validated in this framework (Re < 2500).

4.2. Single scan applied to IN718

The configuration investigated is similar to the first case except that the domain is larger (Fig. 6) with a continuous displacement of the laser with scan velocity v_L of 1 m . s^{-1}. IN718 nickel-based superalloy is investigated as in the previous case. The main interest in this case is to analyse the influence of the vaporisation phenomena on the bead morphology during or after the solidification and in particular the different forces introduced in the momentum conservation equations. Two configurations are investigated. The first one is a ST simulation with the present model introduced in the first part of the paper (case 1). The second one (case 2) is the same simulation without the effects of vaporisation phenomena. Consequently, the heat loss $\dot{q}_v$ (Eq. (14)) in the energy conservation equation (Eq. (6)) and the recoil pressure $\mathbf{f}_V^{\text{RPn}}$ (Eq. (21)) in the momentum conservation equation (16) are ignored. As shown in Fig. 10(a), except from the first interaction to melt the powder, the laser mainly interacts with the melt pool. This observation is consistent with experimental in-situ observations reported in the literature [44,63,64] in a LPBF context regarding standard metallic construction configurations. The two simulations investigated are significantly different in many aspects. The melt pool shape during the simulation as shown in Fig. 10(a,b,c) is deflected for case 1 due to the recoil pressure forces acting on the liquid surface contrary to case 2. In the latter case, the recoil pressure does not counter the surface tension force. The melt pool is consequently bended leading to a convex shape. As previously demonstrated in static shooting, the recoil pressure deforms the melt pool towards the material and allows a better penetration of the laser energy.

This results in a higher penetration and melt pool volume as shown in Fig. 10(a,b). In addition, the maximum temperature reached in case

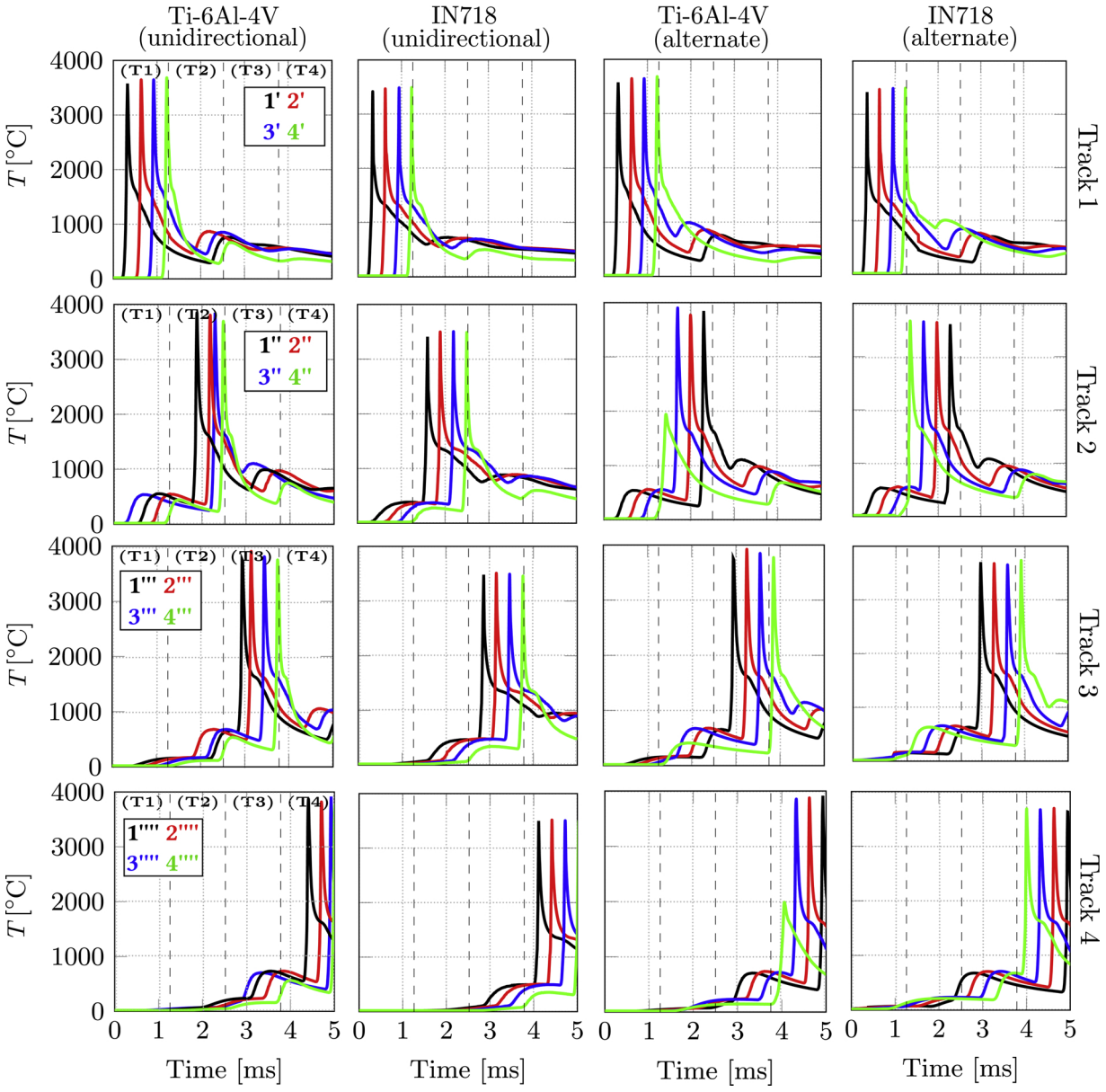

Fig. 13. Temporal evolution of the temperature on local points detailed in Fig. 6 for the different cases investigated.

1 as shown in Fig. 10(c) is almost 1000 °C lower than the one observed in case 2 because of the heat loss induced by vaporisation. When the steady state is reached, approximately at $t = 0.8$ ms as shown in Fig. 10(c), higher temperature gradients are obtained in the case where there is no vaporisation phenomena, leading to stronger Marangoni forces and finally to larger melt pool dimensions. Indeed, the melt pool is deeper but slightly smaller for case 1 than for case 2 as shown in Fig. 10(b) and Table 6. The vaporisation phenomena have a greater influence on the bead depth h_{ms} than it does on the apparent bead height h_{app} as shown in Table 6.

The study of different numbers such as Prandtl, Bond, Reynolds and Marangoni in Table 7 demonstrates that:

- Capillary forces and recoil pressure forces are mainly conducting the melt pool behaviour contrary to buoyancy forces (low Bond number Bo);
- The velocity profile has a low effect on temperature field (low Prandtl number Pr)
- As previously observed in a context of a static laser shooting, the fluid flow is non turbulent (Re < 2500).
- Surface convection generated by the surface tension gradient predominates thermal diffusion and viscosity effects (high Marangoni number Ma).

4.3. Multiple scans applied to IN718 and Ti–6Al–4V

A multiple laser scan configuration is thereafter investigated. This investigation is divided into two tests cases: an unidirectional and an alternate back and forth laser scan strategy as shown in Fig. 6. With respect to single scan tests, the domain sizes are here increased again to ensure that the limit conditions are respected during the computation. The displacement of the laser is still supposed to be continuous corresponding to a scan velocity v_L of 1 m. s^{-1} as indicated in Table 2 (MT case). Furthermore, in addition to the IN718 nickel-based superalloy, a titanium based alloy, Ti–6Al–4V, has been investigated in similar scanning strategies. This comparison may help to reveal the influence of material properties on final bead shape.

4.3.1. Influence of material properties

The influence of material properties is firstly analysed considering

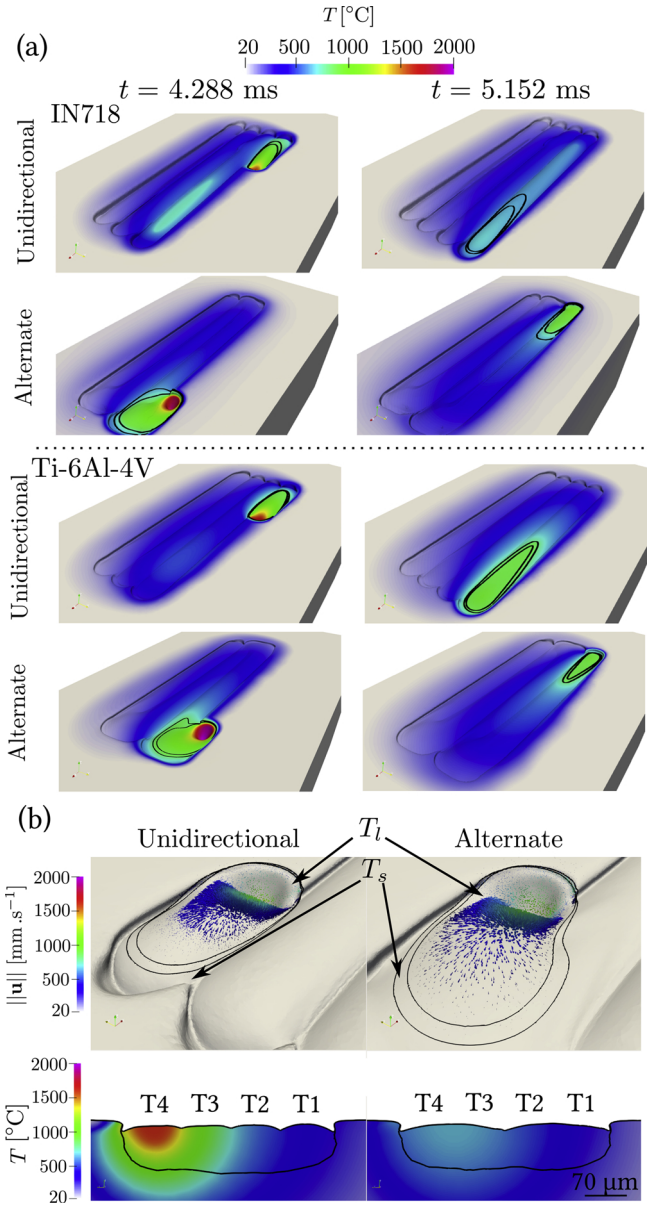

Fig. 14. (a) Temporal evolution of the bead shape with isocontours of liquidus and solidus temperature in black. (b) Comparison on a cross section view at X= 1.25 mm between unidirectional and alternate configuration at the beginning of third track.

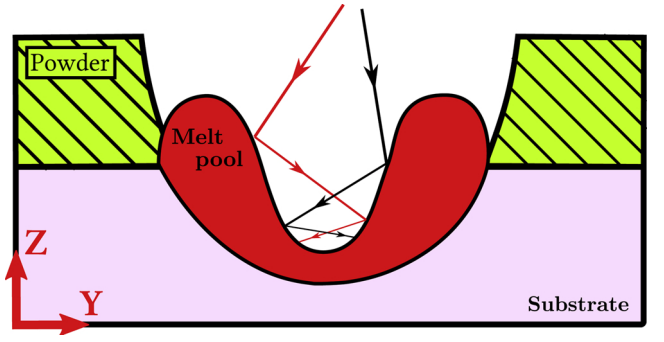

Fig. 15. Schematic of the multiple reflections development into the keyhole geometry.

both scan strategies. A top view of the final state obtained for both materials and of the convection flow close to the keyhole are shown in Fig. 11. The temporal evolution and final dimensions of the bead shape are shown in Fig. 12. The time evolution of temperatures are shown in Fig. 13(b) for local points mentioned in Fig. 6.

As shown in Fig. 12(b-e), a quasi-stationary regime is established from the building of the fourth track. The melt pool enlarges with time for both materials as the whole system is heated continuously (Fig. 12(b)). Larger melt pool volumes are observed for simulations with IN718 powder than with Ti–6Al–4V due to the thermodynamic material properties. More especially, the solidus and liquidus temperatures of the nickel-based material are lower compared to Ti–6Al–4V (Table 1). As shown in Fig. 12(c), the apparent height h_{app} increases since the next track attaches to the substrate on one side and the previous one by surface tension on the other while the first one attached itself only to the substrate.

Furthermore, the progressive rise of the melted zone height h_{ms} (Fig. 12(d)) and the apparent width e_{app} (Fig. 12(e)) are observed in both alloys during multi-scanning process. The temperature encountered track-by-track increases with time because the laser heats a powder that is becoming hotter (Fig. 13) until the quasi-stationary regime is achieved. After the almost complete solidification of the four parallel tracks, as shown in Fig. 11(a), the shape of the bead is influenced by alloy properties. Due to the higher value of surface tension coefficient and a lower Marangoni coefficient for IN718 compared with Ti–6Al–4V (Table 1), the bead shape is more spherical and less wide for simulations with IN718 powder compared with Ti-6Al-4V as shown in Fig. 12(c-e).

Lack of fusion is observed in Fig. 11(a) between the first track and the second one of IN718 alloy since the width of the first track e_{app} is lower than the hatch distance $h_{||}$ fixed for this comparison (Fig. 12(e)). However, this lack of fusion is not observed with Ti–6Al–4V (Fig. 11(a)) because the melt pool width is greater than the hatch distance (Fig. 11(d)). After 4 tracks, the maximum temperature (Fig. 12(a)) and the volume of the melt pool (Fig. 12(b)) begin to stabilise meaning that a quasi-stationary regime is established.

A longitudinal snapshot at $t = 2.432$ ms is shown in Fig. 11(b) in the second track approximately when the melt pool volume is stabilised (or almost stabilised for IN718). The capillary digging is more pronounced on Ti–6Al–4V powder compared with IN718 due to the thermodynamic properties of the materials, also considering the vaporisation temperature and the molar mass of the material. Even if the maximum temperature in the melt pool over time is larger for the case with one Ti–6Al–4V powder than the other material (Fig. 12(a) and Fig. 13), the surface recoil pressure force is nearly the same between the two materials (8.5% greater for IN718 alloy). Nevertheless, the surface tension coefficient is approximately two times larger for IN718 than Ti–6Al–4V. Consequently, the equilibrium between recoil pressure and surface tension force is obtained with a greater value of curvature (Eq. (18)) of the liquid/gas interface for Ti–6Al–4V than IN718. This configuration leads consequently to an increase of the curvature until the equilibrium is reached considering the similar recoil pressure values observed. Therefore, the competition between the two forces is responsible of the more pronounced capillary digging for Ti–6Al–4V than for IN718.

4.3.2. *Influence of the laser scan strategy*

Previous MT simulations were conducted using unidirectional scanning. In this section, different snapshots are also provided in Fig. 14 to demonstrate the influence of the laser scan strategy on the morphology of beads.

As previously demonstrated in Chen's simulations [28], the scan strategy has a significant influence on the final bead shape. In alternate scanning strategy as shown in Fig. 14(a,b), when initiating a new track, the tail of the previous one is still melted in the alternate scanning case contrary to the unidirectional case. This creates an enlarged melt pool at that position. This phenomenon is not observed in unidirectional

scanning strategy as the solidification process is achieved. This phenomenon is not prominent in the context of the construction of a part with long beads of several millimetres since these zones represent a minor proportion of the total bead. Nevertheless, this assumption is not verified in the context of small pillar building of lattice structures where such dimensions of beads must be processed [6]. This configuration of interest justifies the need to investigate the influence of laser scan strategy.

Furthermore, since the dimensions of the beads are small in this context, the previous track is typically at higher temperature than in more traditional built-up part situations. The temperature evolution on local points in Fig. 13 for each material demonstrates that the laser scan strategy has an obvious influence on the temporal temperature distribution. The major difference between the two configurations is that some zones and in particular the beginning and the end of the tracks are not heated at the same time. These zones have a thermal history significantly different with more or less accumulated heat of the previous beads. Consequently, it also implies (Fig. 13) differences both in values of temperature and temperature gradients values in the local points for both alloys investigated. It is well known that these differences influence dramatically the evolution of the microstructure during the solidification of the material. For instance, in the case of Ti–6Al–4V, as shown in Fig. 13, the beta transus temperature is reached for the local point 3' in the alternate scanning configuration whereas it is not achieved in the unidirectional scanning case. This difference is crucial since the beta phase has an influence on the mechanical properties such as the Young modulus or creep resistance [65].

4.3.3. Discussion

For the present simulations, 32 h are required with the continuous-mesoscale model to compute a 1 mm track (parallelised on 56 cores). This time can be compared to the 120 h needed to compute a 0.75 mm track with a particle-mesoscale model as mentioned previously in introduction [25]. Assuming a perfect efficiency of parallelism, and not taking into account the specificity of the cores used, the ratio between the two methods is equal to 3.5, the present continuous-mesoscale being the faster.

For a given set of process, material and numerical parameters and as discussed in the previous section, the first layer of the IN718 simulation contrary to the case with Ti–6Al–4V seems to be not large enough (or the hatch distance is too wide) to get a full dense 4-track layer (Fig. 11(a)). The requirement of not having any unmelted powder between tracks is essential to ensure the good quality of the final part. From this point of view, it should be noticed that the different simulations presented have been achieved with a possible underestimated absorptivity $(1 - R)$ value. Trapp et al. show measurements of the absorptivity for a 316L stainless steel as a function of the laser power for different laser scan velocities [66]. More specifically, for a fixed laser scan velocity, the absorptivity increases as the laser power raises. Obviously, by increasing the laser power, higher temperatures will be reached. The latter will result in stronger recoil pressure and deeper keyhole. Consequently, as shown in Fig. 15, multiple reflections will develop into the keyhole and will finally lead to stronger absorptivity of laser energy [67].

In addition, for a fixed linear energy, when both laser scan velocity and power increase, absorptivity also raises. For higher laser scan velocities, the keyhole tends to be more inclined. This trend is more likely to concentrate the laser rays in the center of the keyhole. Therefore, the temperature in the melt pool will rise and lead to the same conclusions as previously. According to literature [66], a possible more relevant value for the absorptivity would be between 0.65 and 0.75 and not 0.3 as used in the present work.

As a consequence, by increasing the absorptivity (that is decreasing the reflection coefficient R), higher temperatures will be encountered for the two different materials. Larger bead would be observed with stronger recoil pressure providing tracks of expected quality for LBPF process. However, following the results with static laser shooting, a significant rise in temperature will generate a stronger recoil pressure due to higher vaporisation rate. This rise may lead to undesirable gas entrapments. In the framework of the present paper, the purpose of which is to illustrate the response of the model depending on material properties and laser scan strategy, the variation of the absorptivity has been ignored. However, this discussion motivated an ongoing work, consisting in comparing predicted calculated variables with experimental observations and measurements, considering this increase of the absorptivity with the linear energy.

5. Conclusion

In this work, a Level-Set FE method has been used to model AM by powder bed fusion with application to two metallic alloys of industrial interest, the IN718 nickel-based superalloy and the Ti–6Al–4V titanium-based alloy. A volume heat source model is proposed for powder domains based on the work of Chen [5] considering local absorption of the laser energy. Then a surface heat source is used to take into account the absorption of laser energy at the dense matter surface. As the powder bed is assumed as a continuous domain in the present model, a compressible Newtonian law is used to take into account the shrinkage of the powder bed upon melting. A remeshing algorithm is used to ensure a moderate computing time based on error estimation.

Several configurations of variable complexity have been investigated in the present model, providing a better understanding on the influence of vaporisation phenomenon and associated effects. Both vaporisation rate and recoil pressure influence the temperature field evolution in the melt pool and its shape due to the digging of the capillary. The model demonstrated its flexibility when applied to two different materials with distinct scan strategies. Significant gaps are shown in the shape of the obtained melt pool. Future work will be dedicated to the validation of the present model through experiments on bead geometry measurements. Research activities are also in progress aiming to achieve multilayer numerical simulations to investigate the influence of successive bead development.

References

[1] D. Herzog, V. Seyda, E. Wycisk, C. Emmelmann, Additive manufacturing of metals, Acta Mater. 117 (2016) 371–392.
[2] C. Yan, L. Hao, A. Hussein, D. Raymont, Evaluations of cellular lattice structures manufactured using selective laser melting, Int. J. Mach. Tools Manuf. 62 (2012) 32–38.
[3] A. Hussein, L. Hao, C. Yan, R. Everson, P. Young, Advanced lattice support structures for metal additive manufacturing, J. Mater. Process. Technol. 213 (7) (2013) 1019–1026.
[4] L. Murr, S. Gaytan, F. Medina, E. Martinez, J. Martinez, D. Hernandez, B. Machado, D. Ramirez, R. Wicker, Characterization of Ti-6Al-4V open cellular foams fabricated by additive manufacturing using electron beam melting, Mater. Sci. Eng. A 527 (7–8) (2010) 1861–1868.
[5] Y. Chen, P. Cheng, Heat transfer and pressure drop in fractal tree-like microchannel nets, Int. J. Heat Mass Transfer 45 (13) (2002) 2643–2648.
[6] O. Cansizoglu, O. Harrysson, D. Cormier, H. West, T. Mahale, Properties of Ti-6Al-4V non-stochastic lattice structures fabricated via electron beam melting, Mater. Sci. Eng. A 492 (1–2) (2008) 468–474.
[7] X. Wang, S. Xu, S. Zhou, W. Xu, M. Leary, P. Choong, M. Qian, M. Brandt, Y. Xie, Topological design and additive manufacturing of porous metals for bone scaffolds and orthopaedic implants: A review, Biomaterials 83 (2016) 127–141.
[8] S. Biamino, A. Penna, U. Ackelid, S. Sabbadini, O. Tassa, P. Fino, M. Pavese, P. Gennaro, C. Badini, Electron beam melting of Ti-48Al-2Cr-2Nb alloy: Microstructure and mechanical properties investigation, Intermetallics 19 (6) (2011) 776–781.
[9] P. Kobryn, N. Ontko, L. Perkins, J. Tiley, Additive manufacturing of aerospace alloys for aircraft structures, Air Force Research Lab Wright-Patterson AFB OH Materials and Manufacturing, 2006 Tech. rep..
[10] I. Yadroitsev, I. Smurov, Surface morphology in selective laser melting of metal powders, Phys. Proc. 12 (2011) 264–270.
[11] M. Matthews, G. Guss, S. Khairallah, A. Rubenchik, P. Depond, W. King, Denudation of metal powder layers in laser powder bed fusion processes, Acta Mater. 114 (2016) 33–42.
[12] P. Bidare, T. Bitharas, R. Ward, M. Attallah, A. Moore, Fluid and particle dynamics in laser powder bed fusion, Acta Mater. 142 (2018) 107–120.
[13] Mayi, Y. and Dal, M. and Peyre, P. and Bellet, M. and Metton, C. and Moriconi, C.

and Fabbro, R., Laser-induced plume investigated by finite element modelling and scaling of particle entrainment in Laser Powder Bed Fusion (LPBF), Journal of Physics D: Applied Physics (to be published).
[14] Y. Li, D. Gu, Parametric analysis of thermal behavior during selective laser melting additive manufacturing of aluminum alloy powder, Mater. Design 63 (2014) 856–867.
[15] N. Hodge, R. Ferencz, J. Solberg, Implementation of a thermomechanical model for the simulation of selective laser melting, Comput. Mech. 54 (1) (2014) 33–51.
[16] A. Gusarov, I. Yadroitsev, P. Bertrand, I. Smurov, Model of radiation and heat transfer in laser-powder interaction zone at selective laser melting, J. Heat Transfer 131 (7) (2009) 72101.
[17] L. Van Belle, G. Vansteenkiste, J. Boyer, Comparisons of numerical modelling of the selective laser melting, Key engineering materials, Vol. 504, Trans Tech Publ, 2012, pp. 1067–1072.
[18] I. Roberts, C. Wang, R. Esterlein, M. Stanford, D. Mynors, A three-dimensional finite element analysis of the temperature field during laser melting of metal powders in additive layer manufacturing, Int. J. Mach. Tools Manuf. 49 (12–13) (2009) 916–923.
[19] G. Marion, G. Cailletaud, C. Colin, M. Mazière, A finite element model for the simulation of direct metal deposition, International Congress on Applications of Lasers & Electro-Optics (2014) 834–841.
[20] Y. Zhang, G. Guillemot, M. Bernacki, M. Bellet, Macroscopic thermal finite element modeling of additive metal manufacturing by selective laser melting process, Comput. Methods Appl. Mech. Eng. 331 (2018) 514–535.
[21] S. Khairallah, A. Anderson, A. Rubenchik, W. King, Laser powder-bed fusion additive manufacturing: Physics of complex melt flow and formation mechanisms of pores, spatter, and denudation zones, Acta Mater. 108 (2016) 36–45.
[22] A. Martin, N. Calta, S. Khairallah, J. Wang, P. Depond, A. Fong, V. Thampy, G. Guss, A. Kiss, K. Stone, et al., Dynamics of pore formation during laser powder bed fusion additive manufacturing, Nature Commun. 10 (1) (2019) 1987.
[23] C. K“orner, E. Attar, P. Heinl, Mesoscopic simulation of selective beam melting processes, J. Mater. Process. Technol. 211 (6) (2011) 978–987.
[24] M. Bayat, S. Mohanty, J. Hattel, Multiphysics modelling of lack-of-fusion voids formation and evolution in IN718 made by multi-track/multi-layer l-pbf, Int. J. Heat Mass Transfer 139 (2019) 95–114.
[25] A. Aggarwal, S. Patel, A. Kumar, Selective Laser Melting of 316L Stainless Steel: Physics of Melting Mode Transition and Its Influence on Microstructural and Mechanical Behavior, JOM 71 (3) (2019) 1105–1116.
[26] M. Markl, R. Ammer, U. Ljungblad, U. R”ude, C. K“orner, Electron beam absorption algorithms for electron beam melting processes simulated by a three-dimensional thermal free surface lattice boltzmann method in a distributed and parallel environment, Proc. Comput. Sci. 18 (2013) 2127–2136.
[27] T. Mukherjee, H. Wei, A. De, T. DebRoy, Heat and fluid flow in additive manufacturing-part i: Modeling of powder bed fusion, Comput. Mater. Sci. 150 (2018) 304–313.
[28] Q. Chen, G. Guillemot, C.-A. Gandin, M. Bellet, Three-dimensional finite element thermomechanical modeling of additive manufacturing by selective laser melting for ceramic materials, Addit. Manuf. 16 (2017) 124–137.
[29] S. Osher, J. Sethian, Fronts propagating with curvature-dependent speed: algorithms based on hamilton-jacobi formulations, J. Comput. Phys. 79 (1) (1988) 12–49.
[30] M. Rappaz, M. Bellet, M. Deville, Numerical modeling in materials science and engineering, Vol. 32, Springer Science & Business Media, 2010.
[31] O. Desmaison, M. Bellet, G. Guillemot, A level set approach for the simulation of the multipass hybrid laser/GMA welding process, Comput. Mater. Sci. 91 (2014) 240–250.
[32] S. Chen, G. Guillemot, C.-A. Gandin, Three-dimensional cellular automaton-finite element modeling of solidification grain structures for arc-welding processes, Acta Mater. 115 (2016) 448–467.
[33] M. Shakoor, B. Scholtes, P.-O. Bouchard, M. Bernacki, An efficient and parallel level set reinitialization method-application to micromechanics and microstructural evolutions, Appl. Math. Model. 39 (23–24) (2015) 7291–7302.
[34] S. Zhang, G. Guillemot, C.-A. Gandin, M. Bellet, A partitioned two-step solution algorithm for concurrent fluid flow and stress-strain numerical simulation in solidification processes, Comput. Methods Appl. Mech. Eng. 356 (2019) 294–324.
[35] S. Mohanty, J. Hattel, Numerical model based reliability estimation of selective laser melting process, Physics Procedia 56 (2014) 379–389.
[36] H. Willy, X. Li, Z. Chen, T. Herng, S. Chang, C. Ong, C. Li, J. Ding, Model of laser energy absorption adjusted to optical measurements with effective use in finite element simulation of selective laser melting, Mater. Design 157 (2018) 24–34.
[37] J. Li, L. Li, F. Stott, Comparison of volumetric and surface heating sources in the modeling of laser melting of ceramic materials, Int. J. Heat Mass Transfer 47 (6–7) (2004) 1159–1174.
[38] J. Brackbill, D. Kothe, C. Zemach, A continuum method for modeling surface tension, J. Comput. Phys. 100 (2) (1992) 335–354.
[39] C.-C. Tseng, C.-J. Li, Numerical investigation of interfacial dynamics for the melt pool of Ti-6Al-4V powders under a selective laser, Int. J. Heat Mass Transfer 134 (2019) 906–919.
[40] F. Verhaeghe, T. Craeghs, J. Heulens, L. Pandelaers, A pragmatic model for selective laser melting with evaporation, Acta Mater. 57 (20) (2009) 6006–6012.
[41] A. Klassen, T. Scharowsky, C. K”orner, Evaporation model for beam based additive manufacturing using free surface lattice boltzmann methods, J. Phys. D: Appl. Phys. 47 (27) (2014) 275303.
[42] Q. Chen, G. Guillemot, C.-A. Gandin, M. Bellet, Numerical modelling of the impact of energy distribution and marangoni surface tension on track shape in selective laser melting of ceramic material, Addit. Manuf. 21 (2018) 713–723.
[43] W. King, H. Barth, V. Castillo, G. Gallegos, J. Gibbs, D. Hahn, C. Kamath, A. Rubenchik, Observation of keyhole-mode laser melting in laser powder-bed fusion additive manufacturing, J. Mater. Process. Technol. 214 (12) (2014) 2915–2925.
[44] R. Cunningham, C. Zhao, N. Parab, C. Kantzos, J. Pauza, K. Fezzaa, T. Sun, A. Rollett, Keyhole threshold and morphology in laser melting revealed by ultra-high-speed x-ray imaging, Science 363 (6429) (2019) 849–852.
[45] A. Saad, C.-A. Gandin, M. Bellet, Temperature-based energy solver coupled with tabulated thermodynamic properties - application to the prediction of macro-segregation in multicomponent alloys, Comput. Mater. Sci. 99 (2015) 221–231.
[46] T. Tezduyar, S. Mittal, S. Ray, R. Shih, Incompressible flow computations with stabilized bilinear and linear equal-order-interpolation velocity-pressure elements, Comput. Methods Appl. Mech. Eng. 95 (2) (1992) 221–242.
[47] T. Tezduyar, Y. Osawa, Finite element stabilization parameters computed from element matrices and vectors, Comput. Methods Appl. Mech. Eng. 190 (3–4) (2000) 411–430.
[48] S. Gouttebroze, 3D finite element modeling of macrosegregation during solidification of binary alloys, École Nationale Supérieure des Mines de Paris, 2005 PhD thesis.
[49] S. Gouttebroze, M. Bellet, H. Combeau, 3d macrosegregation simulation with anisotropic remeshing, Comptes Rendus Mécanique 335 (5) (2007) 269–279.
[50] E. Hachem, Stabilized finite element method for heat transfer and turbulent flows inside industrial furnaces, Mines ParisTech, 2009 Ph.D. thesis.
[51] E. Hachem, B. Rivaux, T. Kloczko, H. Digonnet, T. Coupez, Stabilized finite element method for incompressible flows with high Reynolds number, J. Comput. Phys. 229 (23) (2010) 8643–8665.
[52] M. Hamide, Modélisation numérique du soudage à l'arc des aciers, Mines ParisTech, 2008 Ph.D. thesis.
[53] M. Khalloufi, Y. Mesri, R. Valette, E. Massoni, E. Hachem, High fidelity anisotropic adaptive variational multiscale method for multiphase flows with surface tension, Comput. Methods Appl. Mech. Eng. 307 (2016) 44–67.
[54] T. Coupez, H. Digonnet, R. Ducloux, Parallel meshing and remeshing, Appl. Math. Model. 25 (2) (2000) 153–175.
[55] T. Coupez, Metric construction by length distribution tensor and edge based error for anisotropic adaptive meshing, J. Comput. Phys. 230 (7) (2011) 2391–2405.
[56] F. Dausinger, J. Shen, Energy coupling efficiency in laser surface treatment, ISIJ Int. 33 (9) (1993) 925–933.
[57] C. Mills, C. Kenneth, Recommended values of thermophysical properties for selected commercial alloys, Woodhead Publishing, 2002.
[58] R. Robert, Simulation numérique du soudage du TA6V par laser YAG impulsionnel: caractérisation expérimentale et modélisation des aspects thermomécaniques associés à ce procédé, Mines ParisTech, 2007 Ph.D. thesis, (in french).
[59] P. Zehner, E.U. Schl“under, W”armeleitf“ahigkeit von Sch”uttungen bei mäßigen Temperaturen, Chemie Ingenieur Technik 42 (14) (1970) 933–941.
[60] E. Lemmon, R. Jacobsen, Viscosity and thermal conductivity equations for nitrogen, oxygen, argon, and air, Int. J. Thermophys. 25 (1) (2004) 21–69.
[61] R. Seban, The Emissivity of Transition Metals in the Infrared, J. Heat Transfer 87 (2) (1965) 173–176.
[62] M. Dal, P. Peyre, V. Gunenthiram, M. Schneider, A new equivalent approach for additive manufacturing (alm) numerical simulation, International Congress on Applications of Lasers & Electro-Optics (2016) 1901.
[63] C. Leung, S. Marussi, R. Atwood, M. Towrie, P. Withers, P. Lee, In situ X-ray imaging of defect and molten pool dynamics in laser additive manufacturing, Nature Commun. 9 (1) (2018) 1355.
[64] M. Pavlov, M. Doubenskaia, I. Smurov, Pyrometric analysis of thermal processes in SLM technology, Physics Procedia 5 (2010) 523–531.
[65] Y. Lee, M. Peters, G. Welsch, Elastic moduli and tensile and physical properties of heat-treated and quenched powder metallurgical Ti-6Al-4V alloy, Metal. Trans. A 22 (3) (1991) 709–714.
[66] J. Trapp, A. Rubenchik, G. Guss, M. Matthews, In situ absorptivity measurements of metallic powders during laser powder-bed fusion additive manufacturing, Appl. Mater. Today 9 (2017) 341–349.
[67] J. Cho, S. Na, Implementation of real-time multiple reflection and fresnel absorption of laser beam in keyhole, J. Phys. D: Appl. Phys. 39 (24) (2006) 5372.